



The MITC3 shell finite element enriched by interpolation covers



Hyeon-Min Jeon^a, Phill-Seung Lee^{a,*}, Klaus-Jürgen Bathe^b

^a Department of Ocean Systems Engineering, Korea Advanced Institute of Science and Technology, 291 Daehak-ro, Yuseong-gu, Daejeon 305-701, Republic of Korea

^b Department of Mechanical Engineering, Massachusetts Institute of Technology, Cambridge, MA 02139, USA

ARTICLE INFO

Article history:

Received 1 August 2013

Accepted 9 December 2013

Available online 28 January 2014

Keywords:

Shell structures
Enriched finite elements
Stress accuracy
MITC shell elements
Interpolation cover
Triangular elements

ABSTRACT

In this paper, we develop a scheme to enrich the 3-node triangular MITC shell finite element by interpolation cover functions. The MITC method is used for the standard and enriched displacement interpolations. The enriched 3-node shell finite element not only captures higher gradients but also decreases inter-elemental stress jumps. In particular, the enrichment scheme increases the solution accuracy without any traditional local mesh refinement. Convergence studies considering a fully clamped square plate problem, cylindrical shell problems, and hyperboloid shell problems demonstrate the good predictive capability of the enriched MITC3 shell finite element, even when distorted meshes are used. We evaluate the effectiveness of the method, and also illustrate the use of the enrichment scheme applied only locally through the solution of two additional shell problems: a shaft–shaft interaction problem and a monster shell problem.

© 2013 Elsevier Ltd. All rights reserved.

1. Introduction

The finite element method is a popular and effective procedure for the analysis of solid, fluid, and multi-physics problems. The key for its success is mainly due to the fact that meshes can be used to span over complicated domain geometries. However, the solution accuracy highly depends on how the geometries are meshed. To obtain reliable solutions with desired accuracy, special mesh refinements are frequently required, in particular, in areas where non-smooth and near-singular solutions are sought [1].

To obtain more accurate solutions, a promising approach is to incorporate special enrichment functions within traditional finite element formulations. For example, Bathe and Chaudhary [2] and Yoon et al. [3] successfully used enriched displacements to analyze warping effects in beam problems. Benzley [4] and Dvorkin et al. [5], Belytschko and Black [6], Moes et al. [7] and Daux et al. [8] employed enrichment functions to account for various singularities in solid mechanics problems. Babuška and Melenk [9] showed in general, mathematically, how to include Ansatz spaces containing the local properties of solutions.

Recently, Kim and Bathe [10] developed and studied a finite element method in which interpolation covers are used. The scheme increases the solution accuracy of the traditional low-order finite element discretization of solids without any changes in the mesh. The major advantage of the method is that the higher order enrichment is available without introducing additional nodes. That is,

traditional nodal point movements or mesh refinements are not used to improve the solution accuracy. The enrichment scheme not only captures higher gradients but also decreases inter-element stress jumps.

Due to discontinuities in geometries (curvature or thickness), incompatibilities of boundary conditions, and irregularities in the loading, shell structures frequently experience stress layers. Within stress layers, the displacements vary rapidly and induce concentrations of strain energies [11,12]. To achieve a desired solution accuracy in such stress layers, a sufficiently fine mesh and/or higher order interpolation functions are required [1]. But the use of traditional mesh refinement procedures can be computationally demanding and tedious for complex shell geometries [13]. In several studies, enrichment functions have been employed for plates and shells, but these studies have focused on special local enrichments near cracks [14–17] rather than on a general enrichment scheme that may be used for various areas of the shell structure.

Displacement-based shell finite elements become too stiff in bending situations when the thickness is relatively small [1]. The phenomenon is called locking. For a long time, there have been numerous attempts to alleviate the locking of plate and shell finite elements [1]. As well established, using the pure displacement-based method in general shell analyses, locking cannot be eliminated [18]. A major advancement has been accomplished by the MITC (Mixed Interpolation of Tensorial Components) method for quadrilateral and triangular plate and shell elements [18–28]. However, a particularly difficult task is to obtain a general 3-node shell element that is effective for the analysis of all shell structures.

* Corresponding author.

E-mail address: phillseung@kaist.edu (P.S. Lee).

The aim of this paper is to develop a 3-node triangular shell finite element enriched by linear interpolation covers within the MITC framework. The key idea is to use and treat the assumed covariant transverse shear strain fields separately for the standard linear and the additional quadratic displacement interpolations. The MITC3 shell finite element enriched by interpolation covers passes the patch tests and shows in example solutions good convergence behavior even when distorted meshes are used. Highly varying stresses in shells can be captured by only locally using interpolation covers.

In the following sections, the finite element procedure to enrich by interpolation covers is briefly reviewed and then the formulation of the enriched MITC3 shell finite element is presented. We discuss the key theoretical and numerical aspects of the scheme regarding the computational expense and the convergence of the method. The results of convergence studies considering a fully clamped square plate problem, cylindrical shell problems, and hyperboloid shell problems are given. Two illustrative example solutions, a shaft–shaft interaction problem and a ‘highly-sensitive’ shell problem, show the effectiveness of using the enriched MITC3 shell finite element also only locally, that is, only in areas of high stress gradients.

2. The finite element method enriched by interpolation covers

Enriching the finite element procedure is in principle, and theoretically, straightforward but difficulties are encountered in obtaining effective schemes [6–10,29–33]. To introduce the basic procedure for the enrichment scheme considered here, let us briefly consider in this section a two-dimensional analysis problem.

Let $\mathbf{Q}^n = \{\mathbf{x}_i\}_{i=1}^n$ be a set of n nodal point position vectors $\mathbf{x}_i = [x_i \ y_i]^T \in \Omega$, and let $\{\lambda_h\} = \{\psi^m\}_{m=1}^q$ be a family of q triangles generated by \mathbf{Q}^n . The triangles correspond to the domain Ω in which we seek the solution variable u

$$\bigcup_{m=1}^q \psi^m = \Omega, \quad (1)$$

The triangles do not overlap, that is, $\psi^j \cap \psi^k = \emptyset$ for $j \neq k$. Fig. 1(a) shows the piecewise interpolation function $h_i(x, y)$ used in the solution. Let C_i be the support domain of h_i , i.e. $C_i = \text{supp}(h_i)$, $\forall i = 1, \dots, N$, which we call the cover region. Hence the cover region C_i corresponds to the union of elements attached to the node i , see Fig. 1(b). For each ψ^m , let $i_c(m)$ be the set of cover indices defined by

$$i_c(m) = \{i : C_i \cap \psi^m \neq \emptyset\}. \quad (2)$$

In Fig. 1, the 3-node triangular element m coincides with the overlapped region of the three cover regions C_i , C_j and C_k and hence $i_c(m) = \{i, j, k\}$. To enrich the standard finite element interpolation for the solution variable u , we use interpolation cover functions

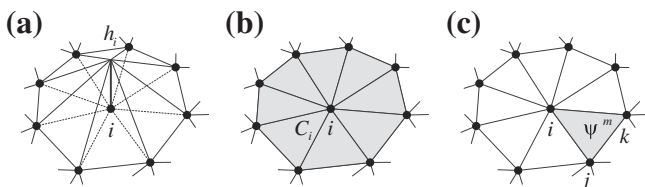


Fig. 1. Description of sub-domain for enriched over interpolations; (a) usual interpolation function, (b) cover region or elements affected by the interpolation cover, and (c) an element.

$$\mathcal{P}_i^p[u] = \bar{u}_i + [\zeta_i \ \eta_i \ \zeta_i^2 \ \zeta_i \eta_i \ \eta_i^2 \ \dots \ \eta_i^p] \hat{\mathbf{u}}_i \text{ with } \zeta_i = \frac{(x-x_i)}{\chi_i}, \ \eta_i = \frac{(y-y_i)}{\chi_i}, \quad (3)$$

where \bar{u}_i is the standard nodal point variable, $\hat{\mathbf{u}}_i = [\hat{u}_i^{\zeta} \ \hat{u}_i^{\eta} \ \hat{u}_i^{\zeta^2} \ \hat{u}_i^{\zeta\eta} \ \hat{u}_i^{\eta^2} \ \dots \ \hat{u}_i^{\eta^p}]^T$ lists the additional degrees of freedom for the cover region, p is the order of the complete polynomial used, and χ_i is the diameter of the largest finite element sharing the node i . The use of χ_i can improve the conditioning of the coefficient matrix.

The enriched approximation for the solution variable is then given by

$$u = \sum_{m=1}^q \sum_{i \in i_c(m)} h_i \mathcal{P}_i^p[u] = \sum_{m=1}^q \left(\sum_{i \in i_c(m)} h_i \bar{u}_i + \sum_{i \in i_c(m)} \mathbf{H}_i \hat{\mathbf{u}}_i \right)$$

$$\text{with } \mathbf{H}_i = h_i [\zeta_i \ \eta_i \ \zeta_i^2 \ \zeta_i \eta_i \ \eta_i^2 \ \dots \ \eta_i^p]. \quad (4)$$

Considering Eq. (4), the enriched cover approximation consists of the standard finite element interpolation plus additional higher order terms. To obtain a well-conditioned stiffness matrix, we use the local coordinate systems (ζ_i, η_i) instead of the global coordinates (x, y) and always (although not mentioned in the example solutions) enforce not only $\bar{u}_i = 0$ but also $\hat{\mathbf{u}}_i = \mathbf{0}$ when imposing the essential boundary conditions at the node i .

The basic properties of the finite element method enriched by interpolation covers were studied for general 2D and 3D finite element analyses in Ref. [10]. These basic properties pertain also to the finite element analysis of shells.

3. The enriched MITC3 shell finite element

In this section, we present the displacement interpolation of the MITC3 shell finite element enriched by the linear interpolation cover. Therefore, the resulting enriched displacement interpolation can give quadratic convergence. We also present the assumed covariant strain fields used for the enriched MITC3 shell finite element.

3.1. Enriched displacement interpolation

The geometry of the 3-node continuum mechanics based triangular shell finite element is interpolated using [23,24,28]

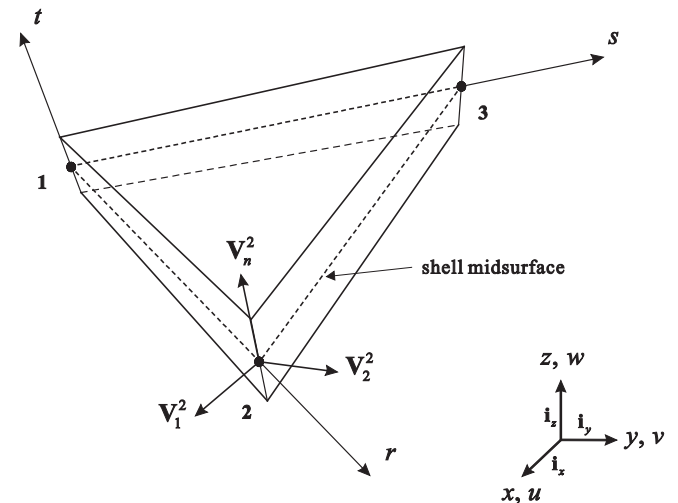


Fig. 2. A 3-node triangular continuum mechanics based shell finite element.

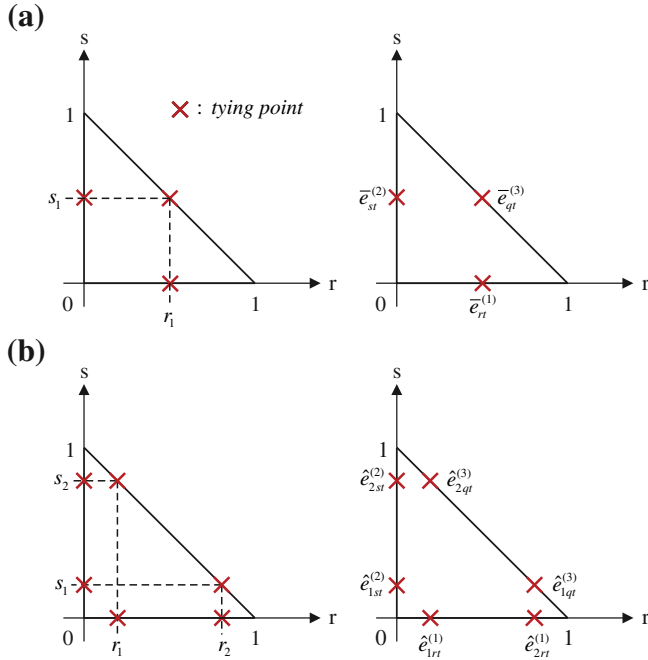


Fig. 3. Tying points for the covariant transverse shear strains of the enriched MITC3 shell finite element: (a) for the standard linear displacement interpolation; $r_1 = s_1 = \frac{1}{2}$, and (b) for the additional quadratic displacement interpolation; $r_1 = s_1 = \frac{1}{2} - \frac{1}{2\sqrt{3}}$ and $r_2 = s_2 = \frac{1}{2} + \frac{1}{2\sqrt{3}}$. Note that the scheme referred to as MITC6b in Ref. [23] is used.

$$\mathbf{x}(r, s, t) = \sum_{i=1}^3 h_i(r, s) \mathbf{x}_i + \frac{t}{2} \sum_{i=1}^3 a_i h_i(r, s) \mathbf{V}_n^i$$

with $h_1 = r$, $h_2 = s$, $h_3 = 1 - r - s$,

(5)

Table 1

Detailed information on the stiffness matrices of the 3-, 6-, and enriched 3-node shell finite elements for the meshes shown in Fig. 4.

	Linear shell element	Quadratic shell elements	
	Standard 3-node	Standard 6-node	Enriched 3-node
Elements	512 ($2N = 16$)	128 ($N = 8$)	128 ($N = 8$)
Nodes	289	289	81
DOFs	803	803	633
Non-zero entries	15,313	24,581	32,797
Half-bandwidth	51	100	83

where r , s , and t are natural coordinates, h_i is the 2D interpolation function corresponding to node i , \mathbf{x}_i is the position vector of node i in the global Cartesian coordinate system, and a_i , \mathbf{V}_n^i denote the shell thickness and the director vector at node i , respectively, see Fig. 2.

The standard displacement interpolation of the shell element is given by

$$\bar{\mathbf{u}} = \sum_{i=1}^3 h_i \bar{\mathbf{u}}_i + \sum_{i=1}^3 \frac{t}{2} a_i h_i \left(-\mathbf{V}_2^i \bar{\alpha}_i + \mathbf{V}_1^i \bar{\beta}_i \right), \quad (6)$$

in which $\bar{\mathbf{u}}_i = [\bar{u}_i \ \bar{v}_i \ \bar{w}_i]^T$ is the nodal displacement vector in the global Cartesian coordinate system, $\mathbf{V}_1^i = [V_{1x}^i \ V_{1y}^i \ V_{1z}^i]^T$ and $\mathbf{V}_2^i = [V_{2x}^i \ V_{2y}^i \ V_{2z}^i]^T$ are unit vectors orthogonal to \mathbf{V}_n^i and to each other, and $\bar{\alpha}_i$ and $\bar{\beta}_i$ are the rotations of the director vector \mathbf{V}_n^i about \mathbf{V}_1^i and \mathbf{V}_2^i at node i .

To enrich the displacement interpolation in Eq. (6), we use the linear interpolation cover, that is, the first order degree of polynomial bases. The enriched displacement interpolation for the 3-node triangular shell finite element is given by

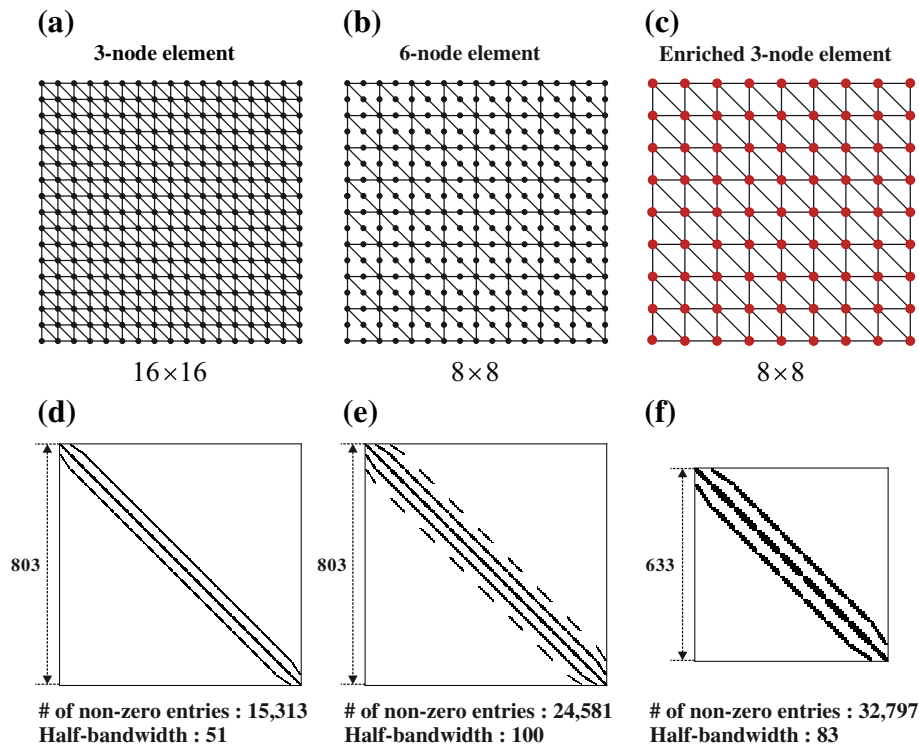


Fig. 4. Meshes used and stiffness matrix structures: (a) and (d) for the 3-node shell element, (b) and (e) for the 6-node shell element, and (c) and (f) for the enriched 3-node shell elements. Non-zero entries are colored in black.

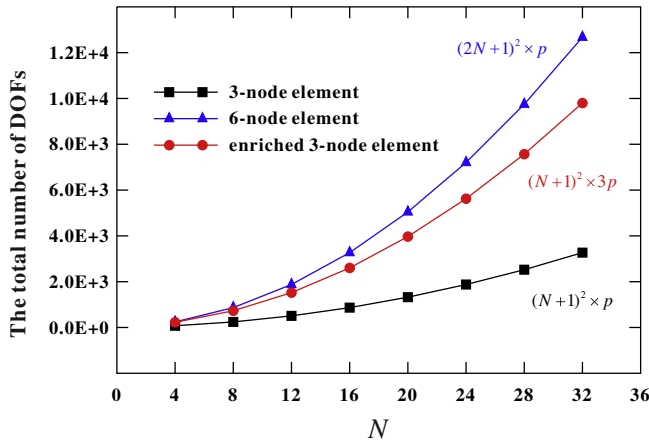


Fig. 5. The total number of degrees of freedom (DOFs) when increasing the number of element layers, N , along an edge p denotes the number of degrees of freedom per node, hence $p = 3$ for the simply supported plate problem.

$$\mathbf{u} = \bar{\mathbf{u}} + \hat{\mathbf{u}} \quad (7)$$

with

$$\hat{\mathbf{u}} = \sum_{i=1}^3 \mathbf{H}_i \hat{\mathbf{u}}_i + \sum_{i=1}^3 \frac{t}{2} a_i \mathbf{H}_i \left(-\mathbf{D}_2^i \hat{\boldsymbol{\alpha}}_i + \mathbf{D}_1^i \hat{\boldsymbol{\beta}}_i \right), \quad (8)$$

in which $\hat{\mathbf{u}}_i = [\hat{u}_i^x \ \hat{u}_i^y \ | \ \hat{v}_i^x \ \hat{v}_i^y \ | \ \hat{w}_i^x \ \hat{w}_i^y]^T$, $\hat{\boldsymbol{\alpha}}_i = [\hat{\alpha}_i^x \ \hat{\alpha}_i^y]^T$ and $\hat{\boldsymbol{\beta}}_i = [\hat{\beta}_i^x \ \hat{\beta}_i^y]^T$ are unknown coefficient vectors for the displacements and rotations, and the \mathbf{H}_i are the linear cover interpolation matrices for the displacements and rotations

$$\mathbf{H}_i = \mathbf{h}_i \begin{bmatrix} \xi_i & \eta_i & 0 & 0 & 0 & 0 \\ 0 & 0 & \xi_i & \eta_i & 0 & 0 \\ 0 & 0 & 0 & 0 & \xi_i & \eta_i \end{bmatrix}, \quad \mathbf{D}_1^i = \begin{bmatrix} V_{1x}^i & 0 \\ 0 & V_{1x}^i \\ V_{1y}^i & 0 \\ 0 & V_{1y}^i \\ V_{1z}^i & 0 \\ 0 & V_{1z}^i \end{bmatrix}, \quad \text{and} \quad \mathbf{D}_2^i = \begin{bmatrix} V_{2x}^i & 0 \\ 0 & V_{2x}^i \\ V_{2y}^i & 0 \\ 0 & V_{2y}^i \\ V_{2z}^i & 0 \\ 0 & V_{2z}^i \end{bmatrix}. \quad (9)$$

Note that the enriched displacement interpolation for \mathbf{u} in Eq. (7) consists of two parts: the standard linear term $\bar{\mathbf{u}}$ and the additional quadratic term $\hat{\mathbf{u}}$.

3.2. Assumed covariant transverse shear strain fields

The covariant strain components are directly obtained as

$$e_{ij} = \frac{1}{2} (\mathbf{g}_i \cdot \mathbf{u}_{,j} + \mathbf{g}_j \cdot \mathbf{u}_{,i}), \quad (10)$$

where $\mathbf{g}_i = \frac{\partial \mathbf{x}}{\partial r_i}$, $\mathbf{u}_{,i} = \frac{\partial \mathbf{u}}{\partial r_i} = \frac{\partial (\bar{\mathbf{u}} + \hat{\mathbf{u}})}{\partial r_i}$ with $r_1 = r$, $r_2 = s$, $r_3 = t$.

Therefore, the enriched covariant strain components are also divided into two parts

$$e_{ij} = \bar{e}_{ij} + \hat{e}_{ij} \quad \text{with} \quad \bar{e}_{ij} = \frac{1}{2} (\mathbf{g}_i \cdot \bar{\mathbf{u}}_{,j} + \mathbf{g}_j \cdot \bar{\mathbf{u}}_{,i}) \quad \text{and} \quad \hat{e}_{ij} = \frac{1}{2} (\mathbf{g}_i \cdot \hat{\mathbf{u}}_{,j} + \mathbf{g}_j \cdot \hat{\mathbf{u}}_{,i}), \quad (11)$$

in which \bar{e}_{ij} and \hat{e}_{ij} correspond to the standard linear and additional quadratic displacement interpolations, respectively.

To alleviate the locking phenomenon, we use the MITC method for the covariant transverse shear strains. However, different assumed covariant transverse shear strain fields are employed for the standard and additional quadratic displacement interpolations. The assumed covariant transverse shear strain fields of the MITC3 and MITC6 shell elements are used for the strains \bar{e}_{ij} and \hat{e}_{ij} , respectively [23]. Note that, in the MITC6 shell element, the covariant membrane strains are also assumed to reduce membrane locking, but this treatment is not necessary and not used for the enriched MITC3 shell element due to its flat geometry.

The assumed covariant transverse shear strain field used for the standard displacement interpolation is [23]

$$\bar{e}_{rt}^{AS} = \bar{e}_{rt}^{(1)} + c s, \quad \bar{e}_{st}^{AS} = \bar{e}_{st}^{(2)} - c r, \quad (12)$$

where $c = \bar{e}_{st}^{(2)} - \bar{e}_{rt}^{(1)} - \bar{e}_{st}^{(3)} + \bar{e}_{rt}^{(3)}$ and, at the tying points, $\bar{e}_{rt}^{(n)}$ and $\bar{e}_{st}^{(n)}$ are calculated from Eq. (11), see Fig. 3(a).

For the additional quadratic displacement interpolation, we use the assumed covariant transverse shear strain field

$$\begin{aligned} \hat{e}_{rt}^{AS} &= a_1 + b_1 r + c_1 s, \\ \hat{e}_{st}^{AS} &= a_2 + b_2 r + c_2 s \end{aligned} \quad (13)$$

and we have the coefficients

$$\begin{aligned} a_1 &= m_{rt}^{(1)} - l_{rt}^{(1)}, \quad b_1 = 2l_{rt}^{(1)}, \quad a_2 = m_{st}^{(2)} - l_{st}^{(2)}, \quad c_2 = 2l_{st}^{(2)}, \\ c_1 &= (a_2 + c_2 - a_1) - (m_{st}^{(3)} + l_{st}^{(3)} - m_{rt}^{(3)} - l_{rt}^{(3)}), \\ b_2 &= (a_1 + b_1 - a_2) + (m_{st}^{(3)} - l_{st}^{(3)} - m_{rt}^{(3)} + l_{rt}^{(3)}) \end{aligned} \quad (14)$$

with

$$m_{jt}^{(i)} = \frac{1}{2} (\hat{e}_{1jt}^{(i)} + \hat{e}_{2jt}^{(i)}), \quad l_{jt}^{(i)} = \frac{\sqrt{3}}{2} (\hat{e}_{2jt}^{(i)} - \hat{e}_{1jt}^{(i)}) \quad \text{with } j = r, s \quad \text{for } i = 1, 2, 3, \quad (15)$$

where $\hat{e}_{1jt}^{(i)}$ and $\hat{e}_{2jt}^{(i)}$ are calculated at the tying points in Fig. 3(b).

We finally obtain the assumed covariant transverse shear strain fields for the enriched MITC3 shell element as

$$e_{jt}^{AS} = \bar{e}_{jt}^{AS} + \hat{e}_{jt}^{AS} = \mathbf{B}_{jt}^{AS} \mathbf{U} \quad \text{with } j = r, s, \quad (16)$$

in which \mathbf{B}_{jt}^{AS} is the covariant transverse shear strain-displacement matrix and \mathbf{U} is the vector that contains the degrees of freedom

Table 2

Solution times (in second) for solving the linear equations. We use $2N \times 2N$ and $N \times N$ meshes for linear and quadratic shell elements, respectively (DOFs: degrees of freedom, HB: half-bandwidth).

N	Linear shell element			Quadratic shell elements					
	Standard 3-node			Standard 6-node			Enriched 3-node		
	DOFs	HB	Time	DOFs	HB	Time	DOFs	HB	Time
4	211	27	0.001	211	52	0.001	177	47	0.001
8	803	51	0.016	803	100	0.016	633	83	0.016
16	3,139	99	0.062	3,139	196	0.125	2,409	155	0.062
32	12,419	195	0.733	12,419	388	1.591	9,417	199	1.045
64	49,411	387	10.70	49,411	772	23.88	37,257	587	15.49

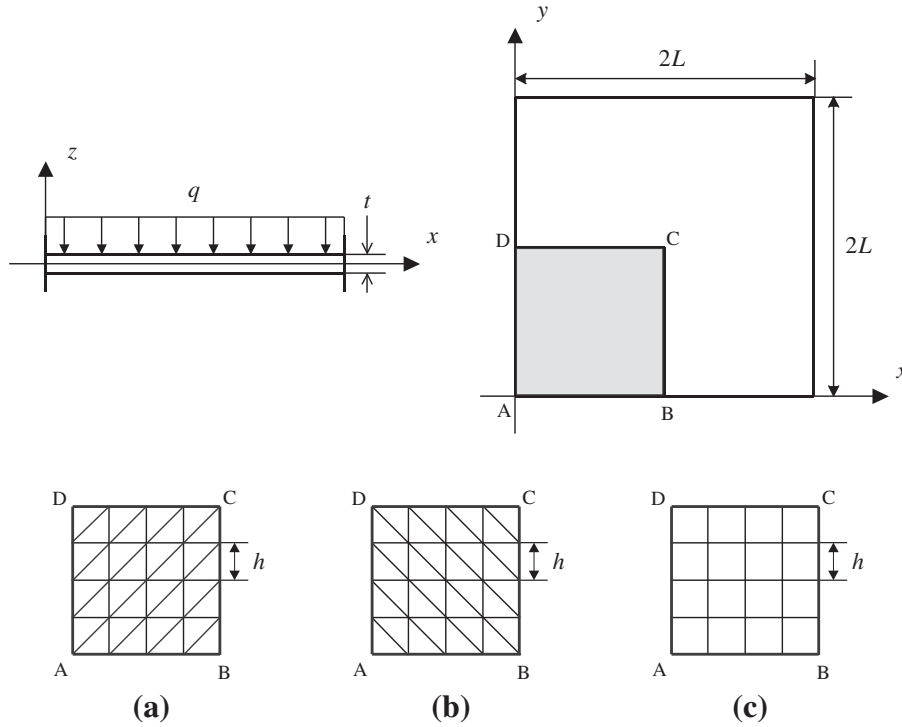


Fig. 6. Fully clamped square plate under uniform pressure ($L = 1.0$, $E = 1.7472 \times 10^7$, $q = 1.0$ and $\nu = 0.3$) with three different 4×4 mesh patterns: (a) and (b) triangular mesh for the MITC3, MITC6 and enriched MITC6 shell elements, and (c) quadrilateral mesh for the MITC4 shell element.

$\bar{\mathbf{u}}_i$, $\bar{\alpha}_i$, $\bar{\beta}_i$ and the additional degrees of freedom $\hat{\mathbf{u}}_i$, $\hat{\alpha}_i$, $\hat{\beta}_i$. Note that we do not use assumed covariant strain fields for other covariant strain components and hence the scheme will not give spurious modes in membrane strains [25,34].

Then, using the appropriate stress–strain matrix for shells, the element stiffness is constructed in the same manner as for the displacement-based shell element [1]. The 7-point Gauss integration is adopted to evaluate the stiffness matrix because the order of the enriched displacement interpolation is quadratic.

Since the cover interpolation is based on the existing nodes, the enriched displacement interpolation can be locally used assigning or not assigning interpolation covers in different regions. Without enrichment, the element is identical to the original MITC3 shell element.

The enriched MITC3 shell element passes the membrane, bending, and transverse shearing patch tests for arbitrary local enrichments, see Refs. [1,18,23,28] for the patch tests performed. Of course, in the tests, the nodal forces corresponding to not only the standard degrees of freedom ($\bar{\mathbf{u}}_i$, $\bar{\alpha}_i$ and $\bar{\beta}_i$) but also the additional degrees of freedom ($\hat{\mathbf{u}}_i$, $\hat{\alpha}_i$ and $\hat{\beta}_i$) must be applied [10].

4. Computational efficiency

In this section, we study some important aspects of the computational efficiency when using the enriched element. The standard 3- and 6-node shell elements (the MITC3 and MITC6 shell elements) and the enriched 3-node shell element (the enriched MITC3 shell element) are considered.

We first study the size and sparseness of the stiffness matrices when using the enriched 3-node shell finite element and the standard 3- and 6-node shell elements for the meshes shown in Fig. 4. A simply supported square plate problem is considered. The meshes used are given in Fig. 4(a)–(c) when $N = 8$. Since the stan-

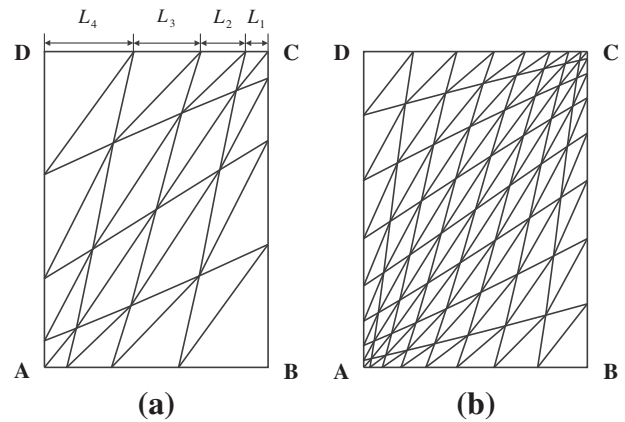


Fig. 7. Distorted meshes used for the fully clamped square plate problem, cylindrical shell problems, and hyperboloid shell problems when (a) $N = 4$ and (b) $N = 8$. The number of triangular elements for an $N \times N$ mesh is $2N^2$.

dard 3-node shell element is based on the linear displacement interpolation, and the 6-node and enriched 3-node shell elements are based on quadratic displacement interpolations, we use a twice finer mesh for the standard 3-node shell element.

The stiffness matrix entries for the simply supported square plate problem for some equivalent mesh patterns are plotted in Fig. 4(d)–(f), where the non-zero entries are colored in black. The size of the stiffness matrices for the meshes used is 803×803 for the 3- and 6-node shell elements and 633×633 for the enriched 3-node shell element. The standard 3- and 6-node shell elements and the enriched 3-node shell element give 15,313, 24,581 and 32,797 non-zero entries in the matrices, respectively. Also, the matrix half-bandwidths are 51, 100 and 83 for the 3- and 6-node shell elements and the enriched 3-node shell element, respectively. Table 1 lists the information regarding these cases.

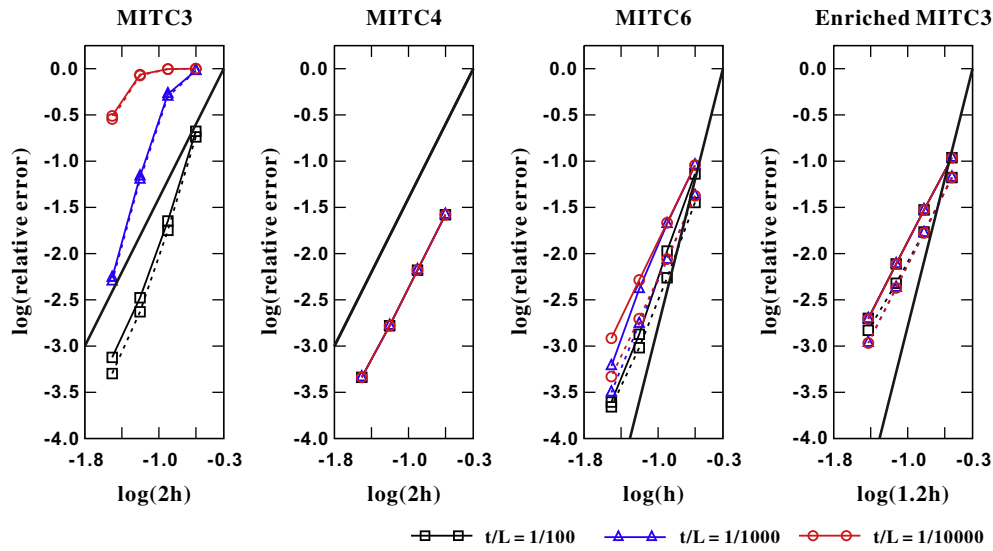


Fig. 9. Convergence curves for the fully clamped square plate problem with uniform meshes. The solid and dotted lines correspond to the results obtained by the mesh patterns in Fig. 6(a) and (b), respectively. The bold line represents the optimal convergence rate, which is 2.0 for linear elements and 4.0 for quadratic elements.

The number of non-zero entries in the stiffness matrix for the enriched 3-node shell element is substantially larger than in the corresponding matrix for the 6-node shell element. This is due to the fact that the support of the higher order interpolation functions in the enriched 3-node shell element is larger than for the 3- and 6-node shell elements. However, using the enriched 3-node shell element, all degrees of freedom are associated with vertex nodes which are shared by several elements and the assembled system of equations is in general smaller than when using the 6-node shell element where edge nodes are only shared by 2 elements. Therefore, the enriched 3-node shell element gives less equations and here also a smaller bandwidth than the 6-node shell element. This fact shows the effectiveness of the enriched 3-node shell element from a computational point of view. Fig. 5 shows how the number of nodal degrees of freedom increases

as a function of the number of elements used in the meshing of Fig. 4.

It is valuable to compare solution times required for the three shell finite elements considered. In all the cases, of course, symmetric stiffness matrices are generated. To obtain more insight into the computational efforts needed in the respective solutions, we focus on the solution of the linear equations using direct Gauss elimination, in which the factorization of the stiffness matrices represents the major expense. To check computational times, we use a quad-core machine (Intel(R) Core i7-3770 CPU @ 3.40 GHz, 8 GB RAM, Windows 7 64bit) for all solution cases. Table 2 shows the solution times for the simply supported square plate problem. As expected, the factorization time for the enriched 3-node shell element is much smaller than for the standard 6-node shell element.

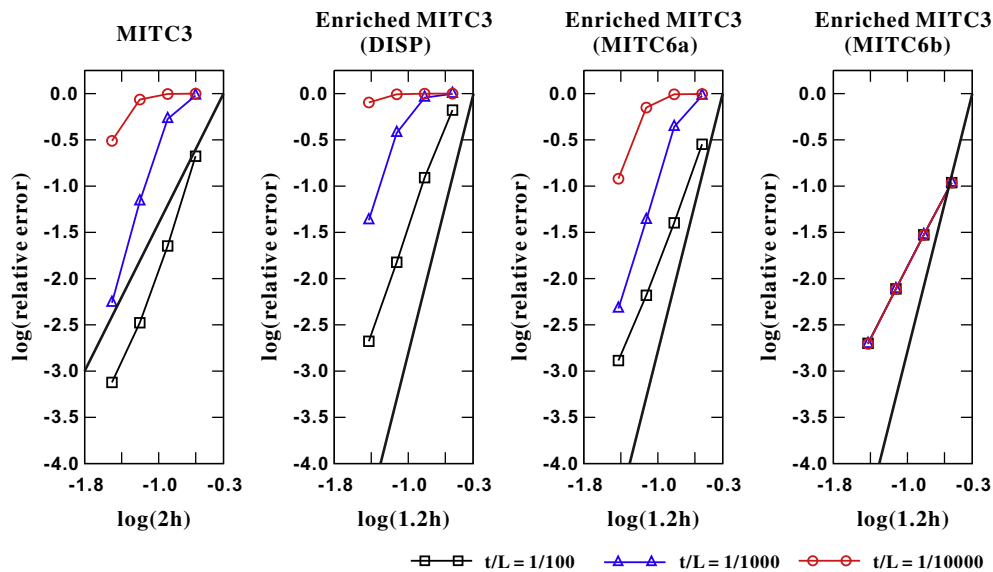


Fig. 8. Convergence curves for the fully clamped square plate problem with uniform meshes. For triangular shell elements, the mesh pattern in Fig. 6(a) is used. The bold line represents the optimal convergence rate, which is 2.0 for linear elements and 4.0 for quadratic elements.

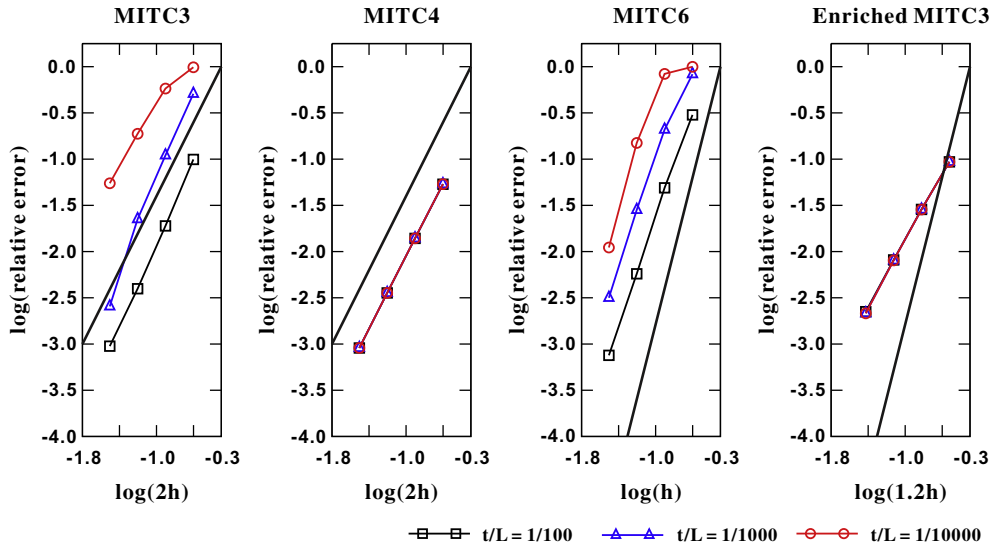


Fig. 10. Convergence curves for the fully clamped square plate problem with the distorted meshes shown in Fig. 7. The bold line represents the optimal convergence rate, which is 2.0 for linear elements and 4.0 for quadratic elements.

5. Convergence studies

In this section, we perform convergence studies on well-established problems for the enriched MITC3 shell element. The solutions can show at most quadratic convergence in the s-norm and the results are compared with those of the MITC3, MITC4, and MITC6 shell elements. We solve various problems: a fully clamped square plate problem, cylindrical shell problems, and hyperboloid shell problems using uniform and distorted meshes [23,24,27,28,35].

The s-norm proposed by Hiller and Bathe [36] is used to measure the convergence of the finite element solutions. The s-norm is suitable to check whether the finite element solutions satisfy consistency and the inf-sup condition [36–40], and is defined as follows

$$\|\mathbf{u} - \mathbf{u}_h\|_s^2 = \int_{\Omega} \Delta \boldsymbol{\varepsilon}^T \Delta \boldsymbol{\tau} d\Omega, \quad (17)$$

where \mathbf{u} is the exact solution, \mathbf{u}_h is the solution obtained using the finite element discretization, $\boldsymbol{\varepsilon}$ and $\boldsymbol{\tau}$ are the strain and stress vectors, and

$$\Delta \boldsymbol{\varepsilon} = \boldsymbol{\varepsilon} - \boldsymbol{\varepsilon}_h, \quad \Delta \boldsymbol{\tau} = \boldsymbol{\tau} - \boldsymbol{\tau}_h. \quad (18)$$

The theoretical convergence behavior can be estimated to be

$$\|\mathbf{u} - \mathbf{u}_h\|_s^2 \cong ch^k, \quad (19)$$

in which c is a constant and h denotes the element size. If a shell element is uniformly optimal, the constant is independent of the shell thickness and k represents the optimal order of convergence, with $k = 2$ for the 3-node shell finite element, and $k = 4$ for the 6-node and the enriched 3-node shell elements.

Instead of the unknown exact solution, a reference finite element solution \mathbf{u}_{ref} calculated using a very fine mesh and a known reliable element can be used, hence Eq. (17) becomes

$$\|\mathbf{u}_{ref} - \mathbf{u}_h\|_s^2 = \int_{\Omega_{ref}} \Delta \boldsymbol{\varepsilon}^T \Delta \boldsymbol{\tau} d\Omega_{ref} \quad \text{with} \quad \Delta \boldsymbol{\varepsilon} = \boldsymbol{\varepsilon}_{ref} - \boldsymbol{\varepsilon}_h, \quad (20)$$

$$\Delta \boldsymbol{\tau} = \boldsymbol{\tau}_{ref} - \boldsymbol{\tau}_h.$$

To measure the convergence of the finite elements in the shell problems, we use the relative error E_h

$$E_h = \frac{\|\mathbf{u}_{ref} - \mathbf{u}_h\|_s^2}{\|\mathbf{u}_{ref}\|_s^2}. \quad (21)$$

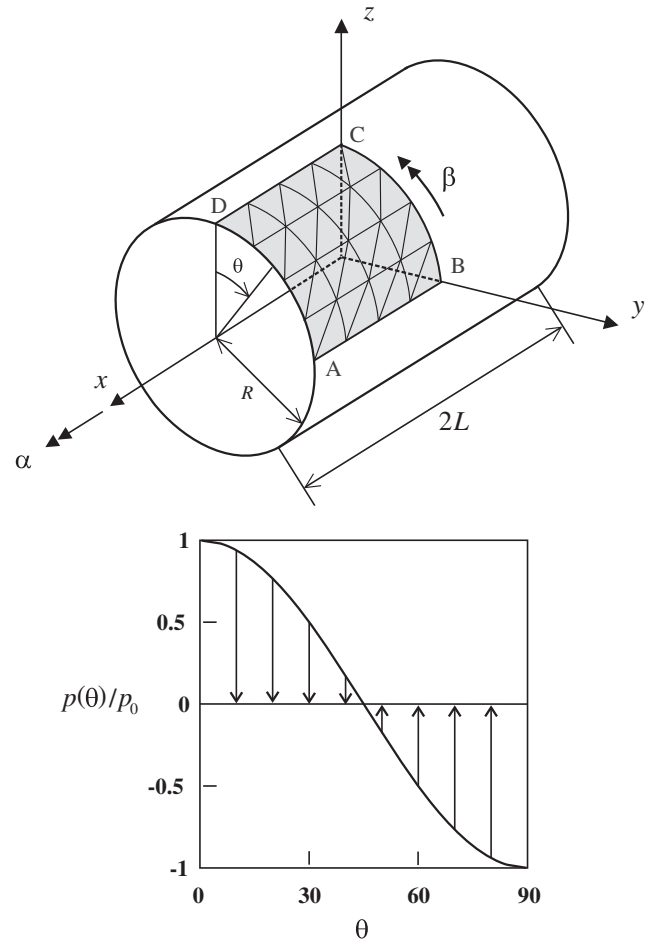


Fig. 11. Cylindrical shell problem (4×4 mesh, $L = R = 1.0$, $E = 2.0 \times 10^5$, $\nu = 1/3$ and $p_0 = 1.0$).

The numerical procedure to calculate the s-norm for shell finite element solutions with general types of elements and general meshes is explained in detail in Ref. [24]. In the use of Eq. (21), it is very

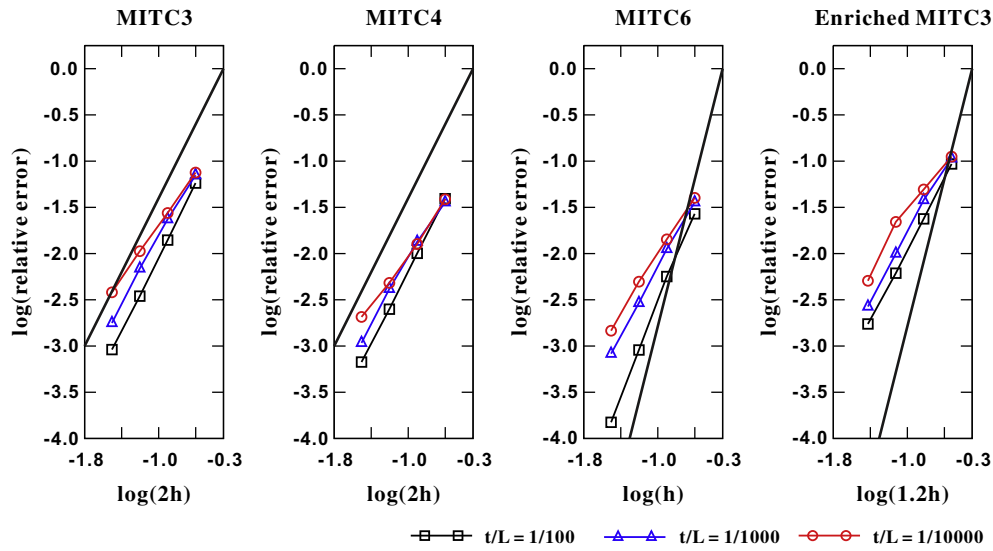


Fig. 12. Convergence curves for the clamped cylindrical shell problem with uniform meshes. The bold line represents the optimal convergence rate, which is 2.0 for linear elements and 4.0 for quadratic elements.

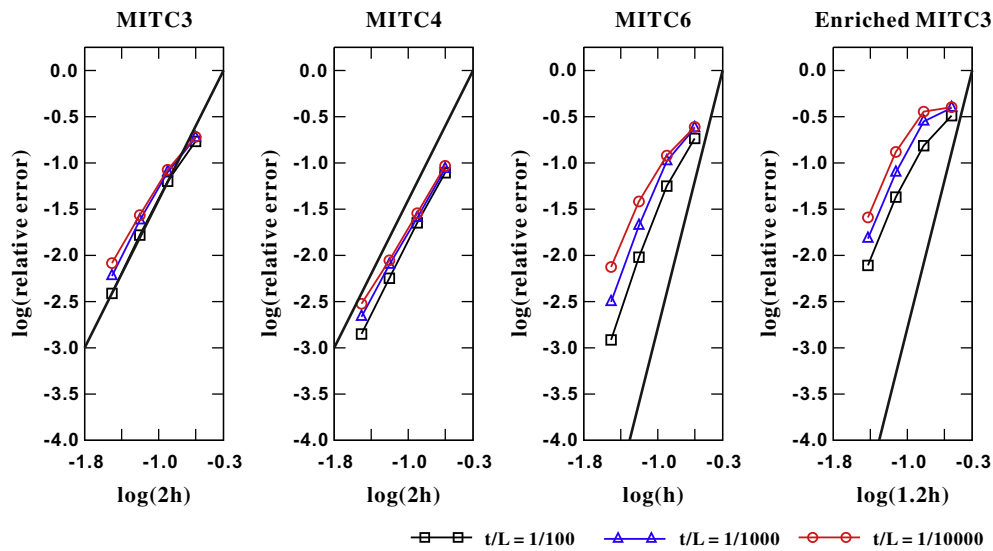


Fig. 13. Convergence curves for the clamped cylindrical shell problem with the distorted meshes shown in Fig. 7. The bold line represents the optimal convergence rate, which is 2.0 for linear elements and 4.0 for quadratic elements.

important to use accurate reference solutions calculated by a reliable shell finite element. In this study, we use well-converged reference solutions calculated using fine meshes of the MITC9 shell finite element. Of course, the MITC9 shell finite element is known to satisfy the ellipticity and consistency conditions and to show adequate convergence behavior, see Refs. [22,35,36].

In the following sections, we present the convergence curves of the MITC3, MITC4, MITC6 shell elements and the fully enriched MITC3 shell element to identify the performance of the enriched MITC3 shell element compared to other shell elements. Note that some convergence curves of the MITC3, MITC4, and MITC6 shell elements have been published before in Refs. [23,24,27].

5.1. Fully clamped square plate problem

The plate problem shown in Fig. 6 is solved. A square plate of size $2L \times 2L$ and constant thickness t is subjected to a uniform

pressure load. Due to symmetry, only one quarter of the plate is modeled, with $\bar{u}_x = \bar{\theta}_y = 0$ along BC, $\bar{u}_y = \bar{\theta}_x = 0$ along DC, and $\bar{u}_x = \bar{u}_y = \bar{u}_z = \bar{\theta}_x = \bar{\theta}_y = 0$ along AB and AD [23,24].

We study the convergence behavior not only using uniform meshes but also distorted meshes, as shown in Fig. 7. When the $N \times N$ distorted mesh is used, each edge is divided by the ratio $L_1 : L_2 : L_3 : \dots, L_N = 1 : 2 : 3 : \dots, N$, leading to quite distorted meshes. The reference solution is obtained with a uniform mesh of 96×96 MITC9 shell finite elements. We use $N = 8, 16, 32$ and 64 for the MITC3 and MITC4 shell elements, and $N = 4, 8, 16$ and 32 for the MITC6 shell element and the enriched MITC3 shell element. Note that in these $N \times N$ meshes N^2 MITC4 elements and $2N^2$ triangular elements are used throughout the paper. Also, in the figures of results we consider the cases $t/L = 1/100, 1/1000$ and $1/10,000$ and use as the “element size” $h = L/N$. To fairly compare convergence behaviors among different shell elements, the equivalent element sizes $2h, h$ and $1.2h$ are used for the MITC3

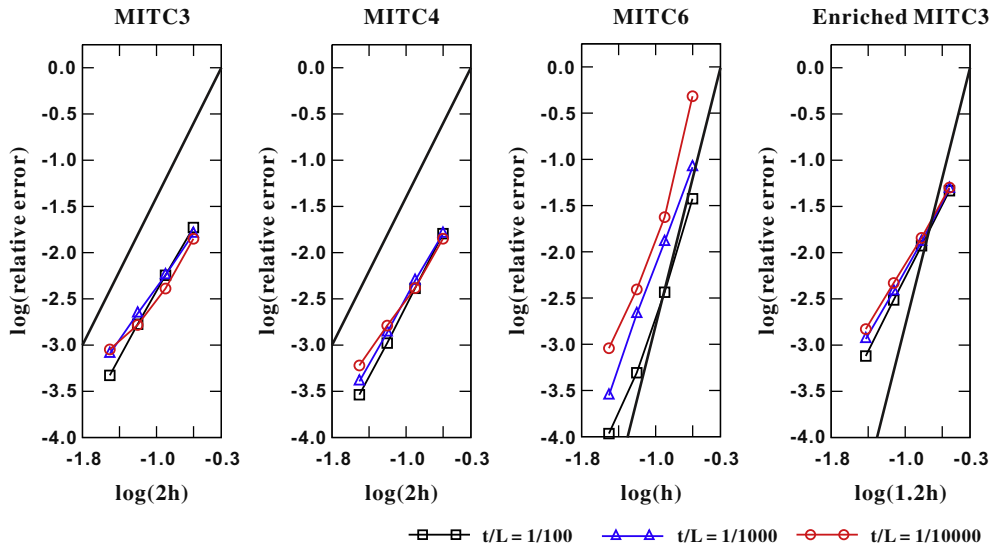


Fig. 14. Convergence curves for the free cylindrical shell problem with uniform meshes. The bold line represents the optimal convergence rate, which is 2.0 for linear elements and 4.0 for quadratic elements.

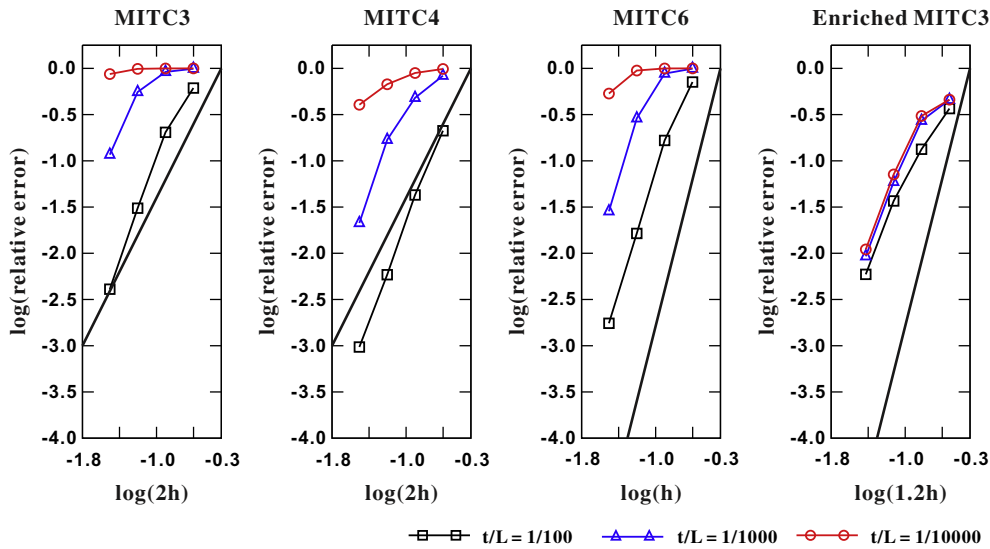


Fig. 15. Convergence curves for the free cylindrical shell problem with the distorted meshes shown in Fig. 7. The bold line represents the optimal convergence rate, which is 2.0 for linear elements and 4.0 for quadratic elements.

and MITC4 shell elements, the MITC6 shell element, and the enriched MITC3 shell element. When using these equivalent element sizes, the numbers of degrees of freedom are similar.

To identify the dependency of the convergence behavior on the MITC scheme chosen for the enriched MITC3 shell element, the following three schemes are considered for the covariant transverse shear strain field of the additional quadratic displacement interpolation:

- No MITC scheme is used (denoted by DISP in Fig. 8).
- The MITC6a scheme is used, for this scheme see Ref. [23].
- The MITC6 scheme in Eq. (13) is used (referred to as MITC6b in Fig. 8)

In all these cases, of course, the MITC3 scheme in Eq. (12) is used for the assumed covariant transverse shear strain field of the standard linear displacement interpolation.

Fig. 8 shows the convergence curves of the original MITC3 shell element and the enriched MITC3 shell elements based on the different assumptions for the transverse shear strain fields. The enriched MITC3 shell element shows different solution accuracy highly depending on the assumed covariant transverse shear strain field used. When the assumed covariant transverse shear strain field of the MITC6 shell element is employed, an almost ideal convergence behavior is observed in this fully clamped square plate problem. Note that the other enriched MITC3 shell elements show an even worse convergence behavior than the original MITC3 shell element. Therefore, in the following sections, we only use the enriched MITC3 shell element based on the MITC6 scheme in Eq. (13).

Figs. 9 and 10 present the convergence curves for the fully clamped square plate problems using uniform and distorted meshes, respectively. The performance of the enriched MITC3 shell element is much better than the performance of the MITC3 and MITC6 shell elements. One reason is probably that the enrichments

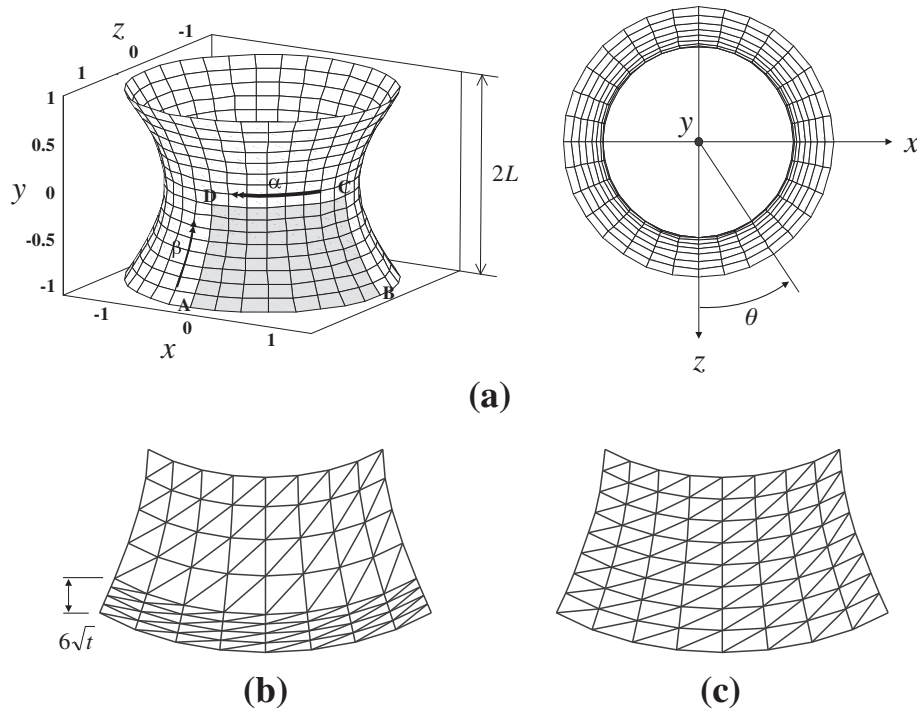


Fig. 16. Hyperboloid shell problem ($E = 2.0 \times 10^{11}$, $\nu = 1/3$ and $p_0 = 1.0$). (a) Shell geometry and boundary conditions, (b) Graded mesh for the clamped case (8×8 mesh, $t/L = 1/1000$), (c) Mesh for the free case (8×8 mesh).

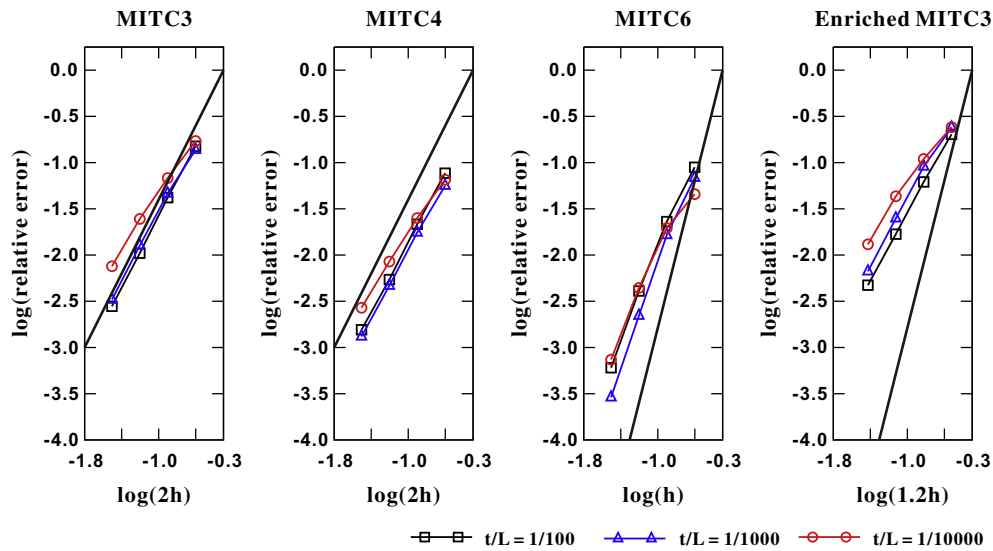


Fig. 17. Convergence curves for the clamped hyperboloid shell problem with uniform meshes. The bold line represents the optimal convergence rate, which is 2.0 for linear elements and 4.0 for quadratic elements.

span over the cover regions and distortions within the regions are not as severe (are smoothed out) in comparison to not using covers. The MITC4 and enriched MITC3 shell finite elements show almost optimal convergence behaviors, even though the distorted meshes are used.

5.2. Cylindrical shell problems

A cylindrical shell with uniform thickness t , length $2L$, and radius R is considered, as shown in Fig. 11. The loading is a smoothly varying periodic pressure $p(\theta)$ normal to the shell surface

$$p(\theta) = p_0 \cos(2\theta). \quad (22)$$

The shell problem gives two different asymptotic behaviors depending on the boundary conditions at both ends: the bending-dominated behavior under free boundary conditions and the membrane-dominated behavior under clamped boundary conditions.

Using the symmetry of the problem, the region ABCD in Fig. 11 is modeled. In the membrane-dominated case, the clamped boundary condition is imposed: $\bar{u}_x = \bar{\beta} = 0$ along BC, $\bar{u}_y = \bar{\alpha} = 0$ along DC, $\bar{u}_z = \bar{\alpha} = 0$ along AB, and $\bar{u}_x = \bar{u}_y = \bar{u}_z = \bar{\alpha} = \bar{\beta} = 0$ along AD. In the bending-dominated case, the free boundary condition

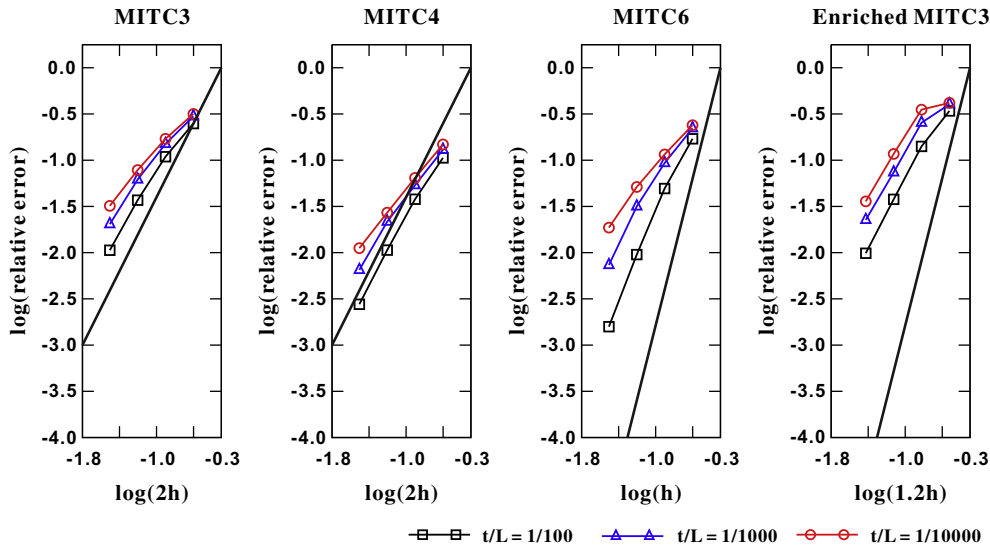


Fig. 18. Convergence curves for the clamped hyperboloid shell problem with the distorted meshes shown in Fig. 7. The bold line represents the optimal convergence rate, which is 2.0 for linear elements and 4.0 for quadratic elements.

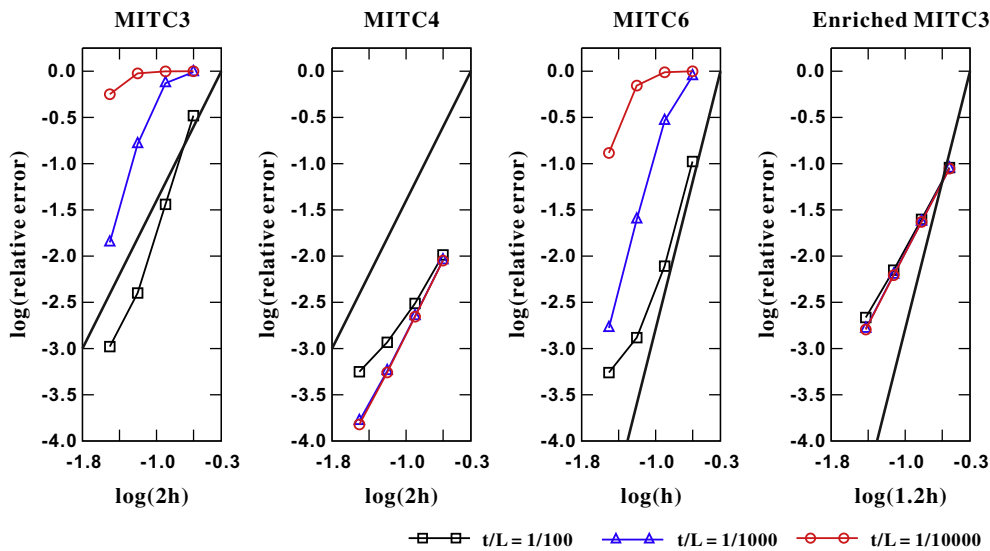


Fig. 19. Convergence curves for the free hyperboloid shell problem with uniform meshes. The bold line represents the optimal convergence rate, which is 2.0 for linear elements and 4.0 for quadratic elements.

is imposed: $\bar{u}_x = \bar{\beta} = 0$ along BC, $\bar{u}_y = \bar{\alpha} = 0$ along DC, and $\bar{u}_z = \bar{\alpha} = 0$ along AB [23].

The reference solution is calculated using a mesh of 96×96 MITC9 shell finite elements for both cases. The solutions using the MITC3, MITC4, MITC6 and enriched MITC3 shell elements are obtained with $N \times N$ meshes ($N = 8, 16, 32$ and 64 for the MITC3 and MITC4 shell elements and $N = 4, 8, 16$, and 32 for the MITC6 and enriched MITC3 shell elements). The element size used in the figures is $h = L/N$. The distorted meshes used are generated as shown in Fig. 7.

Figs. 12 and 13 present the convergence behaviors for the clamped cylindrical shell problems with uniform and distorted meshes, respectively. All the shell finite elements considered show excellent convergence behavior with uniform and distorted meshes.

Figs. 14 and 15 present the convergence curves for the free cylindrical shell problems obtained with uniform and distorted

meshes, respectively. When distorted meshes are used, the solutions of the MITC3, MITC4, and MITC6 shell elements deteriorate as the shell thickness decreases, due to some locking. However, the enriched MITC3 shell element presents good convergence behavior even when using the distorted meshes.

5.3. Hyperboloid shell problems

The hyperboloid shell shown in Fig. 16 is considered, where the midsurface of the shell structure is given by

$$x^2 + y^2 = 1 + y^2; \quad y \in [-1, 1]. \quad (23)$$

A smoothly varying periodic pressure is applied normal to the surface, as in Fig. 11,

$$p(\theta) = p_0 \cos(2\theta), \quad (24)$$

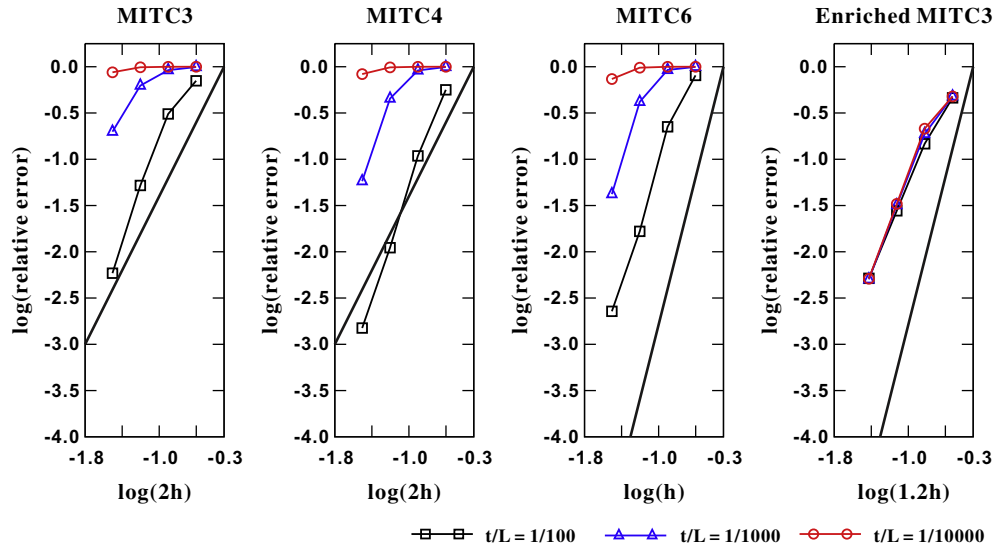


Fig. 20. Convergence curves for the free hyperboloid shell problem with the distorted meshes shown in Fig. 7. The bold line represents the optimal convergence rate, which is 2.0 for linear elements and 4.0 for quadratic elements.

When both ends are clamped, a membrane-dominated problem is obtained, and when the ends are free, a bending-dominated problem is obtained. The bending-dominated hyperboloid shell problem is known to be difficult to solve [23,24,41].

Due to symmetry, the analyses are carried out using one-eighth of the structure, corresponding to the shaded region ABCD in Fig. 16(a). For the membrane-dominated case, the clamped boundary condition is imposed using: $\bar{u}_z = \bar{\beta} = 0$ along BC, $\bar{u}_x = \bar{\beta} = 0$ along AD, and $\bar{u}_y = \bar{\alpha} = 0$ along DC, and $\bar{u}_x = \bar{u}_y = \bar{u}_z = \bar{\alpha} = \bar{\beta} = 0$ along AB. For the bending-dominated case, the free boundary condition is imposed using: $\bar{u}_z = \bar{\beta} = 0$ along BC, $\bar{u}_x = \bar{\beta} = 0$ along AD, and $\bar{u}_y = \bar{\alpha} = 0$ along DC [23,24].

In common with previous problems, we use the reference solutions calculated with a mesh of 96×96 MITC9 shell elements. The solutions using the MITC3, MITC4, MITC6 and enriched MITC3 shell elements are obtained with $N \times N$ meshes ($N = 8, 16, 32$ and 64 for the MITC3 and MITC4 shell elements and $N = 4, 8, 16$, and 32 for the MITC6 and enriched MITC3 shell elements). The element size used in the convergence curves is $h = L/N$. In the clamped hyperboloid shell problem, a boundary layer of width $6\sqrt{t}$ is used for half of the mesh, see Fig. 16(b). In the free hyperboloid shell problem, the thin boundary layer is not specially meshed.

Figs. 17 and 18 show the convergence curves for both uniform and distorted meshes in the membrane dominated case (that is, the clamped hyperboloid shell problem). The performance of all shell elements is good.

For the bending-dominated case (that is, the free hyperboloid shell problem), the convergence curves are shown in Figs. 19 and 20. The enriched MITC3 shell element shows the best convergence behavior among the shell elements considered. Even in the use of distorted meshes, the performance of the enriched MITC3 shell element is excellent while the other shell elements show some degree of locking.

6. Local use of cover interpolations

In the convergence studies given in Section 5, we showed a good performance when the enriched MITC3 shell element is used throughout the mesh. In this section, we illustrate the local use of cover interpolation functions over the solution domains. This scheme of increasing the solution accuracy is quite different from

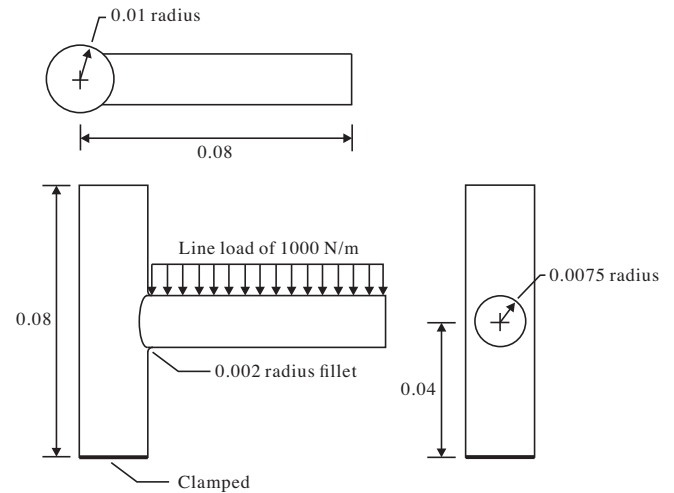


Fig. 21. Shaft-shaft interaction problem with fillets ($E = 2.07 \times 10^{11}$, $\nu = 0.29$).

using conventional standard shell finite elements with mesh refinements. We consider two numerical examples: a shaft-shaft interaction problem and a ‘monster’ shell problem. The maximum effective stress, the strain energy and the deformed shape will be evaluated with and without using local enrichments..

6.1. Shaft-shaft interaction problem

Consider the two cylindrical shafts connected with fillets of radius 0.002 m, in which the horizontal shaft is subjected to a line load of 1000 N/m, as shown in Fig. 21, and the vertical shaft is fully clamped at its lower end [42]. Fig. 22 presents the distribution of the effective stress (von Mises stress) obtained using the MITC4 and MITC3 shell elements, and using the enriched MITC3 shell element throughout the mesh or only locally. The reference solution is given by a fine mesh of the MITC4 shell element, in which 2,150 elements and 10,805 DOFs are used, see Fig. 22(a). Fig. 22(b) presents a finer mesh of the MITC3 shell element and Fig. 22(c)–(e) show the same coarse mesh used for the MITC3 shell

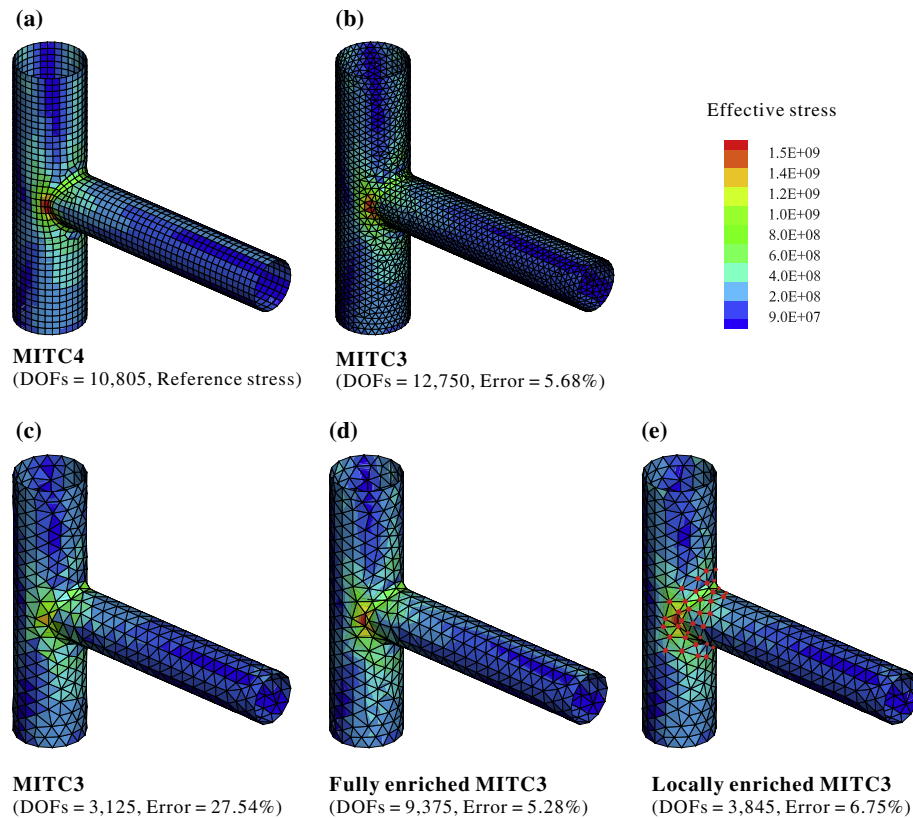


Fig. 22. Distributions of effective stress for the shaft–shaft interaction problem: for (a) the 2,193 node model of the MITC4 shell elements, (b) the 2,582 node model of the MITC3 shell elements, (c) the 641 node model of the MITC3 shell elements, (d) the 641 node model fully enriched, and (e) the 641 node model locally enriched. The red dot represents enriched nodes (DOFs: total number of degrees of freedom used, Error = $(\sigma_v^{ref} - \sigma_v^h) / \sigma_v^{ref} \times 100$). (For interpretation of the references to color in this figure legend, the reader is referred to the web version of this article.)

Table 3
Relative errors in maximum effective stress in the shaft–shaft interaction problem for the five different shell models in Fig. 22. Relative error (%) = $(\sigma_{max}^{ref} - \sigma_{max}^h) / \sigma_{max}^{ref} \times 100$.

	Fine mesh		Coarse mesh		
	MITC4 (reference)	MITC3	MITC3	Fully enriched MITC3	Locally enriched MITC3
Elements	2,150	5,078	1,240	1,240	1,240
Nodes	2,193	2,582	641	641	641
Enriched nodes	–	–	–	641	72
Free DOFs	10,805	12,750	3,125	9,375	3,845
Max. effective stress (σ_{max})	1.78E+09	1.68E+09	1.29E+09	1.69E+09	1.66E+09
Relative error (%)	–	5.68	27.54	5.28	6.75

element and the fully and locally enriched shell models. The red dots in Fig. 22(e) represent the selected nodes carrying interpolation covers around the fillet area where stress concentration is expected.

Table 3 gives the numbers of elements, nodes, degrees of freedom used, and the relative errors in the maximum effective stress obtained when using the shell models in Fig. 22. In the shaft–shaft interaction problem, the maximum effective stress is obtained around the fillet area. Using the local enrichments, the maximum effective stress is well predicted with a much smaller number of degrees of freedom.

6.2. A “highly-sensitive” shell problem

Fig. 23 shows the problem considered (referred to also as “the monster shell problem”) [12]. The shell geometry corresponds to a half-sphere with the top sliced off. The shell is clamped around its entire lower boundary. A smoothly distributed pressure is applied over a small part of the interior of the shell. Since there

is no exact solution to the problem, we use the reference solution given by a fine mesh of 48 (axial) \times 192 (circumferential) MITC4 shell elements; see Fig. 24(a). This is a sufficiently fine mesh to identify and reasonably resolve the boundary layer on the free edge. Fig. 24(b) presents a finer mesh of MITC3 shell elements, and Fig. 24(c)–(e) show a coarser mesh for the MITC3 shell element and the fully and locally enriched cases.

Fig. 24 shows the calculated deformed shapes of the shell when the shell thickness is 0.001 ($t/L = 1/10,000$). For visualization, the displacements are normalized so that the maximum outward total displacement value is equal to 2.0. We note that the displacements are dominant in the immediate vicinity of the free boundary, namely within the boundary layer. Fig. 24(b) and (c) show that the MITC3 shell element meshes are not effective in predicting the displacement oscillations¹ in the circumferential direction within the

¹ In the monster shell problem, the number of displacement oscillations in the boundary layer increases as the shell thickness decreases. The number is given by $\log(L/t)$.

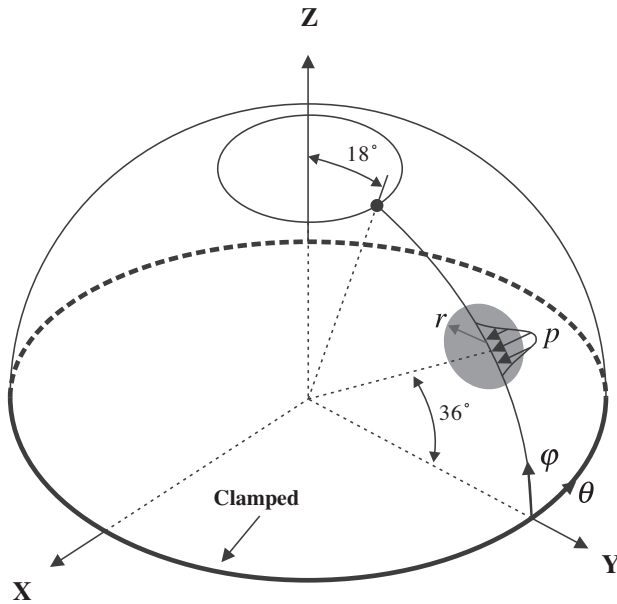


Fig. 23. A “highly-sensitive” shell problem. ($L = R = 10$, $E = 6.285 \times 10^7$, $\nu = 0.3$, and $p(r) = e^{-4r^2}$).

boundary layer. However, when the coarse MITC3 shell element mesh is fully enriched, the displacements in the boundary layer are calculated accurately as shown in Fig. 24(d). Also, the local use of the cover interpolations within the boundary layer results in excellent overall accuracy with a significantly reduced number of degrees of freedom, see Fig. 24(e). Table 4 shows the number of elements, nodes and degrees of freedom used, the number of displacement oscillations, and the relative errors in the strain energies.

7. Conclusions

In this paper, we have proposed a 3-node shell finite element enriched by interpolation covers based on the MITC method. The enriched MITC3 shell finite element is obtained by applying linear displacement interpolation covers to the standard 3-node shell element, and using the MITC procedure. Good convergence behavior in the analysis of various shell problems has been seen, even when distorted meshes are used. The fact that, in the solutions considered, the enriched 3-node element performs sometimes significantly better than the MITC4 and MITC6 shell elements when distorted meshes are used is particularly noteworthy. The effectiveness of using the enrichment scheme only locally was also illustrated by using the cover interpolation functions only in critical areas of an analysis domain.

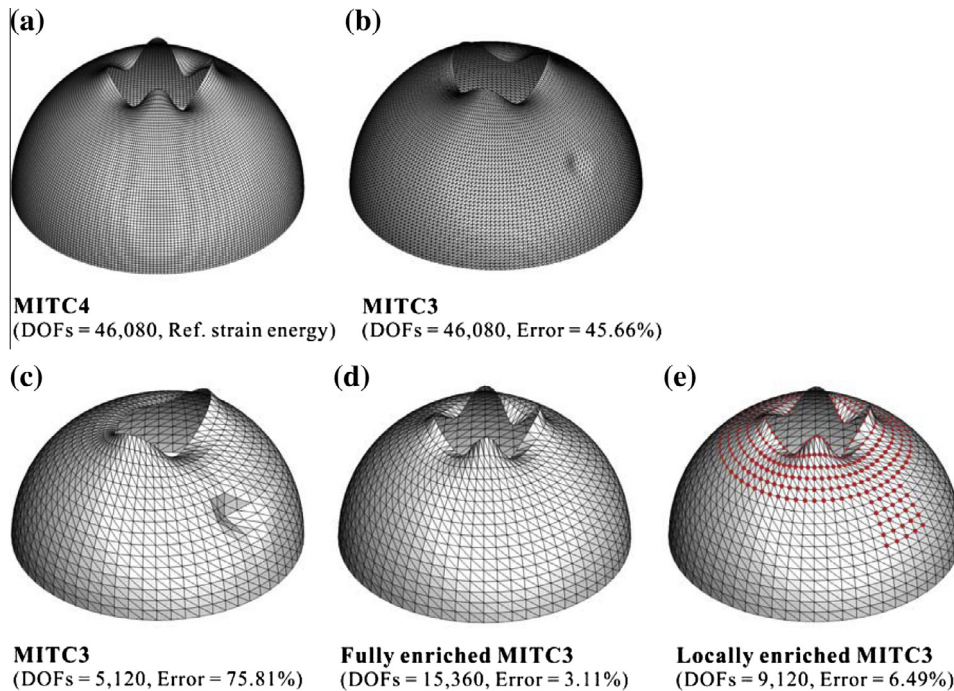


Fig. 24. Deformed shapes for the monster shell ($t/L = 1/10,000$): for (a) the 48 (axial) \times 192 (circumferential) mesh of the MITC4 shell elements, (b) the 48×192 mesh of the MITC3 shell elements, (c) the 16×64 mesh of the MITC3 shell elements, (d) the 16×64 mesh model fully enriched, and (e) the 16×64 mesh model locally enriched. In the figure (e), the red dot represents enriched nodes (DOFs: the total number of degrees of freedom used, Error = $(E_{ref} - E_h)/E_{ref} \times 100$). (For interpretation of the references to color in this figure legend, the reader is referred to the web version of this article.)

Table 4

Relative errors in strain energy in the monster shell problem for the five different shell models in Fig. 24. Relative error (%) = $(E_{ref} - E_h)/E_{ref} \times 100$.

	Fine mesh 48 (axial) \times 192 (circumferential)		Coarse mesh 16 (axial) \times 64 (circumferential)		
	MITC4 (reference)	MITC3	MITC3	Fully enriched MITC3	Locally enriched MITC3
Elements	9,216	18,432	2,048	2,048	2,048
Nodes	9,408	9,408	1,088	1,088	1,088
Enriched nodes	–	–	–	1,088	409
Free DOFs	46,080	46,080	5,120	15,360	9,120
Oscillations	4	3	2	4	4
Strain energy (E)	5.21E–04	2.83E–04	1.26E–04	5.37E–04	4.87E–04
Relative error (%)	–	45.66	75.81	3.11	6.49

We can conclude that cover interpolations and the MITC method are promising schemes for enriching shell element behaviors. Based on the observed good behavior of the enriched MITC3 shell finite element, we expect that an enriched MITC4 shell element will likely also be effective when distorted meshes must be used in areas of shell bending. In future studies, it would be valuable to mathematically analyze the method, to further test the scheme, and to develop the method for nonlinear analysis [1,18,43] and for solving problems containing very high stress gradients, like shell problems containing cracks [32,33,44]. In all of these developments, the ultimate aim should probably be to establish automatic procedures for improving stress solutions [45].

Acknowledgments

This research was supported by the Basic Science Research Program through the National Research Foundation (NRF) of Korea funded by the Ministry of Science, ICT and Future Planning (No. 2011-0014387).

References

- [1] Bathe KJ. Finite element procedures. Cambridge, MA: Klaus-Jürgen Bathe; 2006.
- [2] Bathe KJ, Chaudhary A. On the displacement formulation of torsion of shafts with rectangular cross-sections. *Int J Numer Methods Eng*. 1982;18:1565–8.
- [3] Yoon KH, Lee YG, Lee PS. A continuum mechanics based 3-D beam finite element with warping displacements and its modeling capabilities. *Struct Eng Mech* 2012;43–4:411–37.
- [4] Benzley S. Representation of singularities with isoparametric finite elements. *Int J Numer Methods Eng* 1974;8:537–45.
- [5] Dvorkin EN, Cuitiño AM, Gioia G. Finite elements with displacement interpolated embedded localization lines insensitive to mesh size and distortions. *Int J Numer Methods Eng* 1990;30(3):541–64.
- [6] Belytschko T, Black T. Elastic crack growth in finite elements with minimal remeshing. *Int J Numer Methods Eng* 1999;45:601–20.
- [7] Moes N, Dolbow J, Belytschko T. A finite element method for crack growth without remeshing. *Int J Numer Methods Eng* 1999;46:131–50.
- [8] Daux C, Moes N, Dolbow J, Sukumar N, Belytschko T. Arbitrary branched and intersecting cracks with the extended finite element method. *Int J Numer Methods Eng* 2000;48:1741–60.
- [9] Babuška I, Melenk JM. The partition of unity method. *Int J Numer Methods Eng* 1997;40:727–58.
- [10] Kim J, Bathe KJ. The finite element method enriched by interpolation covers. *Comput Struct* 2013;116:35–49.
- [11] Lee PS, Bathe KJ. On the asymptotic behavior of shell structures and the evaluation in finite element solutions. *Comput Struct* 2002;80(3–4):235–55.
- [12] Bathe KJ, Chapelle D, Lee PS. A shell problem 'highly-sensitive' to thickness changes. *Int J Numer Methods Eng* 2003;57(8):1039–52.
- [13] Bathe KJ, Zhang H. A mesh adaptivity procedure for CFD & fluid–structure interactions. *Comput Struct* 2009;87:604–17.
- [14] Areias PM, Belytschko T. Non-linear analysis of shells with arbitrary evolving cracks using XFEM. *Int J Numer Methods Eng* 2005;62:384–415.
- [15] Areias PM, Song JH, Belytschko T. Analysis of fracture in thin shells by overlapping paired elements. *Comput Method Appl Mech* 2006;195:5343–60.
- [16] Wyart E, Coulon D, Duflot M, Pardoën T, Remacle J-F, Lani F. A substructured FE-shell/XFE-3D method for crack analysis in thin-walled structures. *Int J Numer Methods Eng* 2007;72:757–79.
- [17] Zhuo Z, BinBin C. A novel enriched CB shell element method for simulating arbitrary crack growth in pipes. *Sci China Phys Mech Astron* 2011;54:1520–31.
- [18] Dvorkin EN, Bathe KJ. A continuum mechanics based four-node shell element for general nonlinear analysis. *Eng Comput* 1984;1:77–88.
- [19] Bathe KJ, Dvorkin EN. A formulation of general shell elements – the use of mixed interpolation of tensorial components. *Int J Numer Methods Eng* 1986;22:697–722.
- [20] Brezzi F, Bathe KJ, Fortin M. Mixed-interpolated elements for Reissner/Mindlin plates. *Int J Numer Methods Eng* 1989;28:1787–801.
- [21] Bucalem ML, Bathe KJ. Higher-order MITC general shell elements. *Int J Numer Methods Eng* 1993;36:3729–54.
- [22] Bathe KJ, Lee PS, Hiller JF. Towards improving the MITC9 shell element. *Comput Struct* 2003;81:477–89.
- [23] Lee PS, Bathe KJ. Development of MITC isotropic triangular shell finite elements. *Comput Struct* 2004;82:945–62.
- [24] Lee PS, Noh HC, Bathe KJ. Insight into 3-node triangular shell finite elements: the effects of element isotropy and mesh patterns. *Comput Struct* 2007;85:404–18.
- [25] Beirão da Veiga L, Chapelle D, Paris Suarez I. Towards improving the MITC6 triangular shell element. *Comput Struct* 2007;85:1589–610.
- [26] Bucalem ML, Bathe KJ. The mechanics of solids and structures – hierarchical modeling and the finite element solution. Springer; 2011.
- [27] Chapelle D, Bathe KJ. The finite element analysis of shells – fundamentals. 2nd ed. Berlin: Springer; 2011.
- [28] Lee Y, Yoon K, Lee PS. Improving the MITC3 shell finite element by using the Hellinger-Ressner principle. *Comput Struct* 2012;110–111:93–106.
- [29] Shi GH. Manifold method of material analysis. In: *Trans. 9th Army Conf. on Applied Mathematics and Computing*; 1991. p. 57–76.
- [30] Strouboulis T, Copps K, Babuška I. The generalized finite element method. *Comput Methods Appl Mech Eng* 2001;190:4081–193.
- [31] Tian R, Yagawa G, Terasaka H. Linear dependence problems of partition of unity-based generalized FEMs. *Comput. Methods Appl. Mech. Eng* 2006;195:4768–82.
- [32] Hong WT, Lee PS. Coupling flat-top partition of unity method and finite element method. *Finite Elem Anal Des* 2013;67:43–55.
- [33] Hong WT, Lee PS. Mesh based construction of flat-top partition of unity. *App Math Comput* 2013;219:8687–704.
- [34] Kim DN, Bathe KJ. A triangular six-node shell element. *Comput Struct* 2009;87:1451–60.
- [35] Lee PS, Bathe KJ. The quadratic MITC plate and MITC shell elements in plate bending. *Adv Eng Software* 2010;41:712–28.
- [36] Hiller JF, Bathe KJ. Measuring convergence of mixed finite element discretizations: an application to shell structures. *Comput Struct* 2003;81:639–54.
- [37] Bathe KJ, Iosilevich A, Chapelle D. An inf-sup test for shell finite elements. *Comput Struct* 2000;75:439–56.
- [38] Chapelle D, Bathe KJ. The mathematical shell model underlying general shell elements. *Int J Numer Methods Eng* 2000;48:289–313.
- [39] Bathe KJ. The inf-sup condition and its evaluation for mixed finite element methods. *Comput Struct* 2001;79:243–52.
- [40] Bathe KJ, Lee PS. Measuring the convergence behavior of shell analysis schemes. *Comput Struct* 2011;89:285–301.
- [41] Lee PS, Bathe KJ. Insight into finite element shell discretizations by use of the "basic shell mathematical model". *Comput Struct* 2005;83:69–90.
- [42] ADINA Primer: ARD 12-7, ADINA R & D Inc., Watertown, MA; December 2012.
- [43] Sussman T, Bathe KJ. 3D-shell elements for structures in large strains. *Comput Struct* 2013;122:2–12.
- [44] Thanh CD, Zi G, Lee PS, Rabczuk T, Song JH. Phantom-node method for shell models with arbitrary cracks. *Comput Struct* 2012;92–93:242–56.
- [45] Kim J, Bathe KJ. Towards a procedure to automatically improve finite element solutions by interpolation covers. *Comput Struct* 2014;131:81–97.